PAPER

Check for updates

Anisotropic ultrahigh hole mobility in two-dimensional penta-SiC$_2$ by strain-engineering: electronic structure and chemical bonding analysis

Yuanfeng Xu,[a] Zeyu Ning,[a] Hao Zhang, [ID] *[ac] Gang Ni,[a] Hezhu Shao, [ID] [b] Bo Peng, [ID] [a] Xiangchao Zhang,[a] Xiaoying He,[a] Yongyuan Zhu[c] and Heyuan Zhu[a]

Monolayer pentagonal silicon dicarbide is a 2D material composed entirely of pentagons, and it possesses novel electronic properties possibly leading to many potential applications. In this paper, using first-principles calculations, we have systematically investigated the electronic, mechanical and transport properties of monolayer penta-SiC$_2$ by strain-engineering. By applying in-plane tensile or compressive strain, it is possible to modulate the physical properties of monolayer penta-SiC$_2$, which subsequently changes the transport behaviour of the carriers. More interestingly, at room temperature, the uniaxial compressive strain of -8% along the a-direction can enhance the hole mobility of monolayer penta-SiC$_2$ along the b-direction by almost three orders of magnitude up to 1.14×10^6 cm^2 V^{-1} s^{-1}, which is much larger than that of graphene, while similar strains have little influence on the electron mobility. The ultrahigh and strain-modulated carrier mobility in monolayer penta-SiC$_2$ may lead to many novel applications in high-performance electronic and optoelectronic devices.

1 Introduction

Two-dimensional (2D) materials have attracted great attention in the fields of nanoscale materials and nanotechnology since the experimental realization of graphene,[1–3] which possesses remarkable mechanical, electronic and optical properties[4–7] possibly leading to many novel applications in microelectronic and optoelectronic devices. A number of graphene-like layered structures with different chemical compositions and different crystal structures have been proposed and synthesised since then.[8–10] Recently, Zhang *et al.*[11] predicted a new 2D material composed entirely of carbon pentagons, *i.e.* penta-graphene, formed by the mixed sp^2/sp^3 orbital hybridization of C atoms, which was proven to be dynamically and mechanically stable, and can withstand temperatures as high as 1000 K.[11] Monolayer penta-graphene possesses an unusual negative Poisson's ratio, an ultrahigh ideal strength outperforming graphene and other interesting electronic properties,[11,12] which make it a potential candidate for wide applications in optoelectronics and photovoltaics devices.

Many efforts have been devoted to the discovery of new 2D materials with a penta structure since the successful prediction of penta-graphene.[13,14] The silicon counterpart of the penta structure was proposed as well, although it is dynamically unstable in the monolayer form.[15] Recently, a novel pentagonal structure composed of carbon and silicon atoms formed by sp^{2}d hybridization, *i.e.* pentagonal silicon dicarbide (penta-SiC$_2$), has been proposed and further confirmed to be dynamically stable and exhibits enhanced similar electronic properties compared to penta-graphene.[16]

However, during the processes of experimental realization of 2D materials like monolayer penta-SiC$_2$, the mismatch between the 2D material and the substrate often results in the formation of crystal distortion due to strain or stress modulation, also called straintronics.[17,18] Experimental results have shown that strains of up to 11% are possible for monolayer MoS$_2$ in an AFM indentation experiment without bond breaking.[19,20] Therefore it is necessary to investigate the strain-dependence properties of 2D materials with the purpose of comparison with experimental results. In addition, strain-engineering (external strain and stress) is an effective way to modulate the electronic, mechanical, optical and transport properties of 2D materials.[21–25] It has been reported that strain-engineering can be used to modulate the electronic properties of MoS$_2$,[26] black phosphorene,[27] TiS$_3$ (ref. 28) and ReS$_2$.[23] The strain-engineering method was proven to be effective in increasing the band gap of penta-SiC$_2$ (ref. 16) as well.

In this work, we have systematically investigated the electronic, mechanical and transport properties of monolayer penta-SiC$_2$ under tensile and compressive strain by using first-principles calculations. We found that under in-plane uniaxial

[a]Department of Optical Science and Engineering, Key Laboratory of Micro and Nano Photonic Structures (Ministry of Education), Fudan University, Shanghai 200433, China. E-mail: yuanfengxu15@fudan.edu.cn; zhangh@fudan.edu.cn

[b]Ningbo Institute of Materials Technology and Engineering, Chinese Academy of Sciences, Ningbo 315201, China

[c]Nanjing University, National Laboratory of Solid State Microstructure, Nanjing 210093, China

strain, penta-SiC$_2$ remains an indirect semiconductor up to a tensile strain of 22%, however, the uniaxial compressive strain can easily convert it from semiconducting into metallic. When applying a biaxial strain, penta-SiC$_2$ can change from a semiconductor to a metallic material under a relatively low compressive strain of −8%. In general, the electronic band structure of penta-SiC$_2$ is sensitive to tensile and compressive strain. Moreover, we quantitatively demonstrated that the carrier mobility can be enhanced from 2.59×10^3 cm^2 V^{-1} s^{-1} to 1.14×10^6 cm^2 V^{-1} s^{-1} by applying a uniaxial compressive strain.

2 Method and computational details

The calculations were performed using the Vienna *ab initio* simulation package (VASP) based on density functional theory.[29] The exchange–correlation energy was described by the generalized gradient approximation (GGA) using the Perdew–Burke–Ernzerhof (PBE) functional. The calculations were carried out by using the projector-augmented-wave pseudo potential method with a plane wave basis set with a kinetic energy cutoff of 500 eV. When optimizing atomic positions, the energy convergence value between two consecutive steps was chosen as 10^{-5} eV and the maximum Hellmann–Feynman force acting on each atom is 10^{-3} eV Å^{-1}. The Monkhorst–Pack scheme was used for the Brillouin zone integration with k-point meshes of $13 \times 13 \times 1$ and $21 \times 21 \times 1$ for geometry optimization and self-consistent electronic structure calculations, respectively.

To verify the results of the PBE calculations, the electronic structure of penta-SiC$_2$ with zero strain was calculated using the hybrid Heyd–Scuseria–Ernzerhof (HSE06) functional.[30] HSE06 improves the precision of the band gap calculation by reducing the localization and delocalization errors of the PBE and HF functionals. The mixing ratio used in the HSE06 is 25% for a short-range Hartree–Fock exchange. The screening parameter is set to be 0.2 Å^{-1}. In order to extract the Wannier functions associated with the bands near the Fermi level, the commonly adopted procedure for maximizing the localization of Wannier functions (MLWFs) has been performed using the WANNIER90 code.[31,32] The interface between VASP and WANNIER90 was used for the calculations of the MLWF projection.

3 Results and discussion

3.1 Electronic band structure and bonding analysis of strained penta-SiC$_2$

The top and side views of the fully optimized structure of penta-SiC$_2$ are shown in Fig. 1(a) and (b), respectively. The unit cell (the red dashed rectangle) contains two silicon atoms and four carbon atoms. The optimized penta-SiC$_2$ has a tetragonal crystal structure with the $p\bar{4}21m$ space group. As shown in Fig. 1(a) and (b), all pentagons contain four equivalent Si–C bonds and one C–C bond located within three atomic layers (two C atom layers on the top and bottom, and a Si atom layer in the middle). As shown in Table 1, the associated lattice constant of penta-SiC$_2$ is $a = b = 4.41$ Å with the buckling height $h = 1.33$ Å. The bonding lengths are $d_1 = 1.91$ Å and $d_2 = 1.36$ Å, which are in good

agreement with previous theoretical results.[33] To avoid artificial interactions between atom layers, the separation between the layers is set to be 15 Å for monolayer penta-SiC$_2$.

The PBE calculations show that SiC$_2$ is a semiconductor with an indirect band gap of 1.39 eV, and the maximum of the valence band (VBM) is located at the S point, and the minimum of the conduction band (CBM) is located between the S and Γ points. The corresponding HSE06 calculation gives a larger band gap of 2.85 eV compared to the PBE result since PBE always underestimates the value of the band gap of semiconductors. Fig. 1(c) shows the PBE calculated electronic band structures and the density of states (DOS) of penta-SiC$_2$. Analysis of the PDOS (Si-3s and 3p and C-2s and 2p orbitals) of penta-SiC$_2$ reveals that the C-2p and Si-3p orbitals mainly dominate the electronic states near the Fermi level. However, the contributions from the C-2p states to the total DOS are larger than those from Si-3p, and in the energy range of −2 to 0 eV for the valence band, the Si-3p states contribute more than the C-2p states, indicating the strong hybridization between the Si-3p states and the C-2p states. The analysis of the chemical bonding of penta-SiC$_2$ based on the DOS is consistent with the calculated bond lengths and bond angles. The four identical bond lengths and bond angles indicate that the fourfold coordinated Si atom connects to the four neighboring C atoms *via* sp^{2}d-like hybridization,[34] although the Si and C atom layers are in different planes, as shown in Fig. 1(b). The chemical bonding analysis of the threefold coordinated C atoms shows that C connects to the two neighboring Si atoms and one C atom *via* a mixed combination of sp^2 and sp^3 hybridization, reflected by the bond angles shown in Table 1.

According to the chemical bond analysis of the monolayer penta-SiC$_2$, the band structure near the Fermi level has been calculated based on the projected MLWFs associated with the sp^{2}d-like hybrid orbitals of the fourfold coordinated Si atoms and the sp^2 hybrid orbitals of the threefold coordinated C atoms, which fits quite well with the band structure calculated by the standard PBE method based on the plane-wave pseudopotential method, as shown in Fig. 1(b). The aforementioned analysis of the chemical bonds can be reflected by the contour surface plots of the MLWF as well, which is shown in Fig. 2(a) and (d). Only the MLWFs for the 10th and 11th bands near the Fermi level labeled in Fig. 1(c) are shown here.

The isosurface plot of the MLWF associated with the valence band, shown in Fig. 2(b), reveals that the sp^{2}d-like hybridization states of the fourfold coordinated Si atom connecting to the surrounding C atoms determine the valence band of monolayer penta-SiC$_2$, and the p$_z$ state of the C atoms also plays an important role. The chemical covalent sp^{2}d-like bond becomes stronger along the L_1 direction, shown in Fig. 1(a), when a compressive uniaxial strain of −10% along the a-direction is applied, due to the shorter Si–C bond length, which is shown in Fig. 2(b). However, when applying a tensile uniaxial strain of 10% along the a-direction, the distance of L_1 increases further than that of L_2, which attenuates the chemical Si–C bonding, especially along the L_1 direction. It is shown in Fig. 2(c) that the Si–C bonds along the L_2 direction still form sp^{2}d-like hybridization patterns, however, the bonding characteristic of Si–C along the L_1 direction becomes very weak and changes
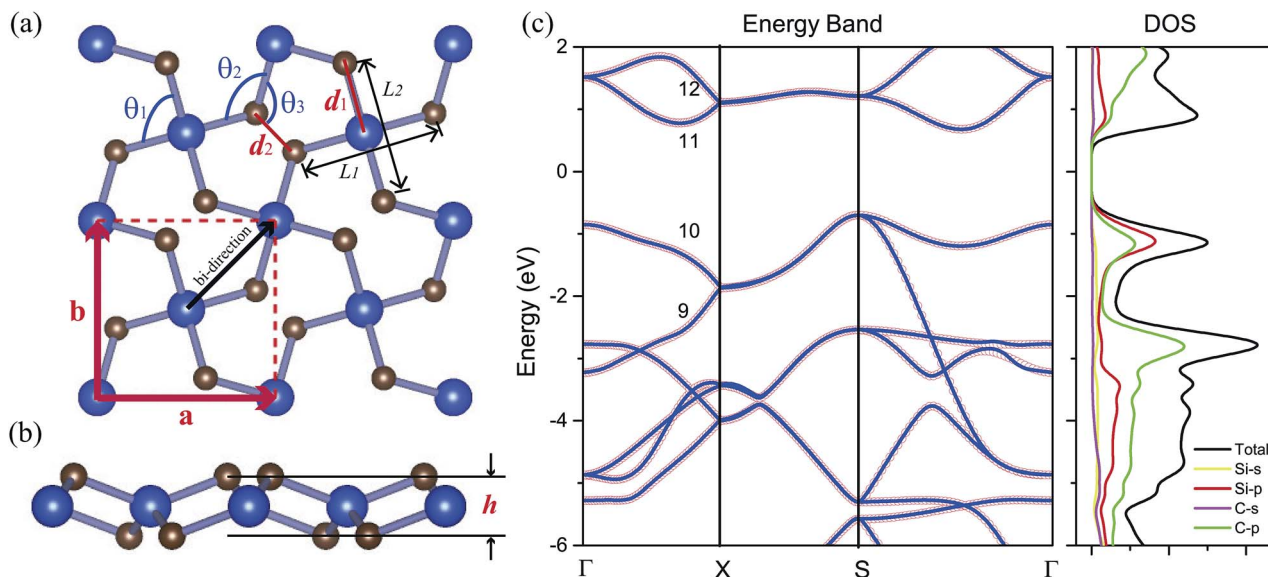
Fig. 1 (a) The top view and (b) side view of the atomic structure of the penta-SiC$_2$ monolayer (2 × 2 supercell). d_1 and d_2 are the bond lengths of Si−C and C−C in this pentagonal structure, respectively. θ_1, θ_2 and θ_3 are the bond angles. h is the buckling distance. (c) PBE calculations of the electronic band structures (red circles) of monolayer penta-SiC$_2$ in comparison to the MLWF-based fitting bands (blue lines), and the density of states (DOS) of penta-SiC$_2$.

Table 1 The calculated structure properties of 2D penta-SiC$_2$: buckling distance (h), Si−C and C−C bond lengths (d_1, d_2), bond angles (C−Si−C: θ_1, Si−C−Si: θ_2 and Si−C−C: θ_3), the band gap calculated by PBE and HSE06 respectively, and the Young's modulus (Y)

h [Å]	d_1 [Å]	d_2 [Å]	θ_1 [°]	θ_2 [°]	θ_3 [°]	E_g (PBE/HSE06) [eV]	Y (GPa)
1.33	1.91	1.36	96.94	109.57	117.40	1.39/2.85	292
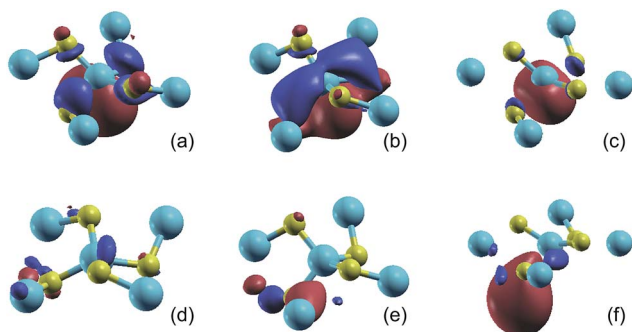
Fig. 2 The isosurface plots (iso-value = 2.0) of the MLWFs for penta-SiC$_2$ without strain (a and d), with a uniaxial compressive strain of −10% along the a-direction (b and e), and with a uniaxial tensile strain of 10% along the a-direction (c and f). The MLWFs of (a–c) and (d–f) are associated with the 10th and 11th band, respectively. The band index is labeled in Fig. 1(b).

obviously. Therefore, the compressive and tensile strains applied to the monolayer penta-SiC$_2$ will distort the lattice and subsequently change the chemical bonding of the Si and C atoms along the directions normal to each other.

The isosurface plot of the MLWF associated with the conduction band, shown in Fig. 2(d), reveals that the sp antibonding states of the threefold coordinated C atoms contribute mainly to the total energy of monolayer penta-SiC$_2$, and the antibonding characteristic does not change for the strained penta-SiC$_2$ when a compressive uniaxial strain of −10% along the a-direction is applied, as shown in Fig. 2(e). However, the tensile strain of 10% along the a-direction stretches the lattice and the chemical bonds of the threefold coordinated C atoms become a π^*_{pp} antibonding state, as shown in Fig. 2(f).

Fig. 3 shows the evolution of the valence and conduction band structures as a function of different strains, mainly from −10% to 10% of the fully relaxed structure. Fig. 3(a) and (b) show the dependence of the energy bands of monolayer penta-SiC$_2$ on strain along the a- and bi-directions, respectively. The shift of the band edge as shown in Fig. 3(a) and (b) can be understood in terms of the bonding and antibonding states,[35] as described above. The monolayer penta-SiC$_2$ is an indirect semiconductor described by the VBM of V_S and the CBM of $C_{S-\Gamma}$. Under uniaxial compressive strain, $C_{S-\Gamma}$ decreases while V_S increases, leading to a shrinking indirect band gap of the strained penta-SiC$_2$. The reason why the formation of the indirect band gap of compressively-strained penta-SiC$_2$ remains unchanged is due to the fact that the characteristics of the chemical bonding and antibonding states of the compressive penta-SiC$_2$, which are shown in Fig. 2(b) and (e), respectively, for −10% strain, stay unchanged when a compressive strain is applied, according to the aforementioned bonding analysis.

However, by applying a uniaxial tensile strain, the characteristics of both the chemical bonding and antibonding states of the stretched penta-SiC$_2$ change, which is shown in Fig. 2(c) and (f), respectively, for 10% strain, thus the corresponding band energies change greatly, which transforms the stretched
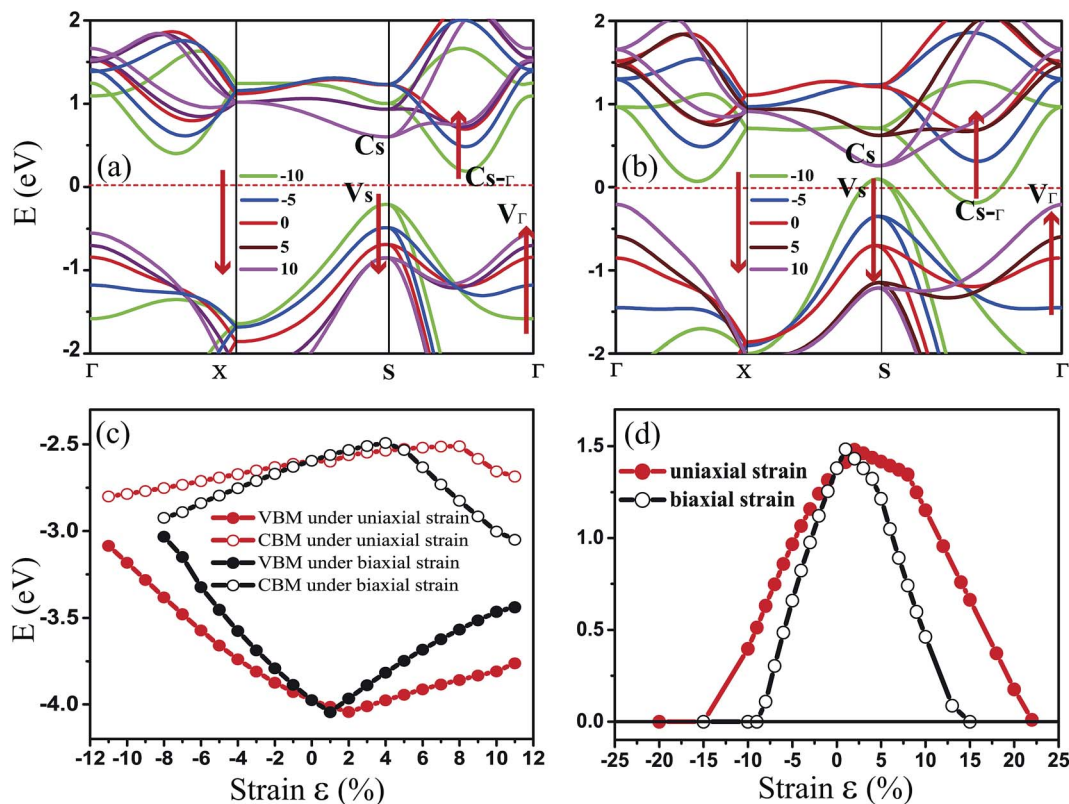
Fig. 3 The PBE calculated band structures under (a) uniaxial (*a*-direction) strain and (b) biaxial (bi-direction) strain for penta-SiC$_2$. (c) shows the change of the CBM/VBM with the applied uniaxial (ε_x) and biaxial (ε_{xy}) strains. (d) shows the evolution of the band gap for penta-SiC$_2$ as a function of ε_x and ε_{xy}.

penta-SiC$_2$ into a new type of indirect semiconductor formed by the VBM of V_Γ and the CBM of C_S.

While for an external strain along the bi-direction (ε_{xy}), large changes take place for the energies corresponding to V_S, V_Γ, C_S and $C_{S-\Gamma}$, as shown in Fig. 3(b). When $\varepsilon_{xy} = -8\%$, the semiconductor (indirect)-to-metal transition takes place. The strain tunable electronic structure of monolayer SiC$_2$ will significantly influence the electronic transport properties, which can be used in electronic and optoelectronic applications.

Fig. 3(c) and (d) show the evolution of the calculated band edges (CBM/VBM) and the band gap under various strains. When applying the in-plane uniaxial strain of $-15\% \leq \varepsilon_x \leq 22\%$, penta-SiC$_2$ remains an indirect semiconductor with a maximum band gap of 1.481 eV at 2%, while the gap values and the positions of the VBM and CBM change. However, when applying the in-plane biaxial strain of $-15\% \leq \varepsilon_{xy} \leq 15\%$, penta-SiC$_2$ also retains the indirect semiconducting feature, and it converts into a metal beyond 15% and -9%. The band
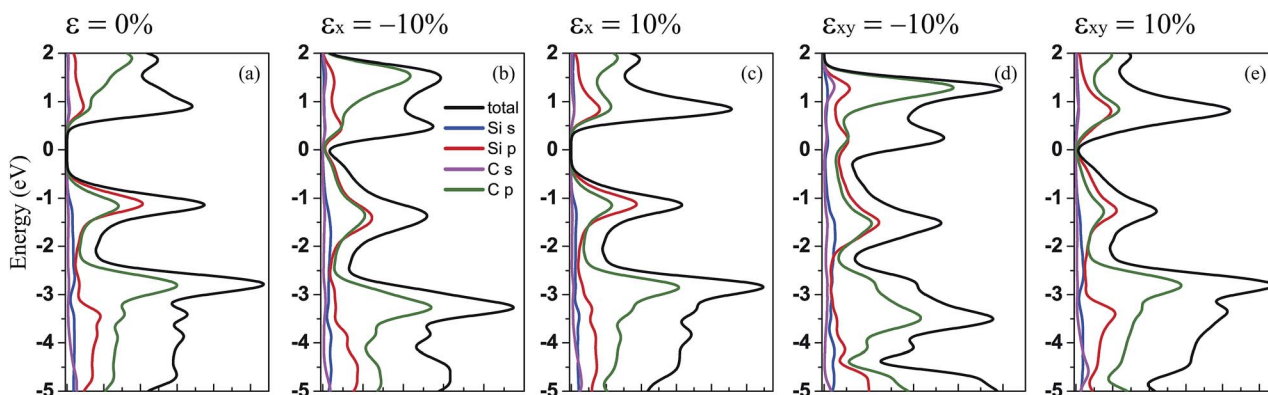

Fig. 4 The PBE calculated total and partial density of states for penta-SiC$_2$ under uniaxial and biaxial strain with compressive and tensile strength: (a) no strain, (b) $\varepsilon_x = -10\%$, (c) $\varepsilon_x = 10\%$, (d) $\varepsilon_{xy} = -10\%$, and (e) $\varepsilon_{xy} = 10\%$.
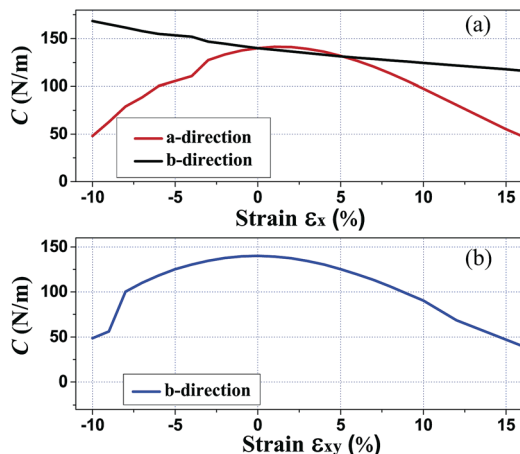
Paper

Fig. 5 The calculated elastic modulus C_{ij}^{2D} along the a- and b-directions under various mechanical strains for penta-SiC$_2$.
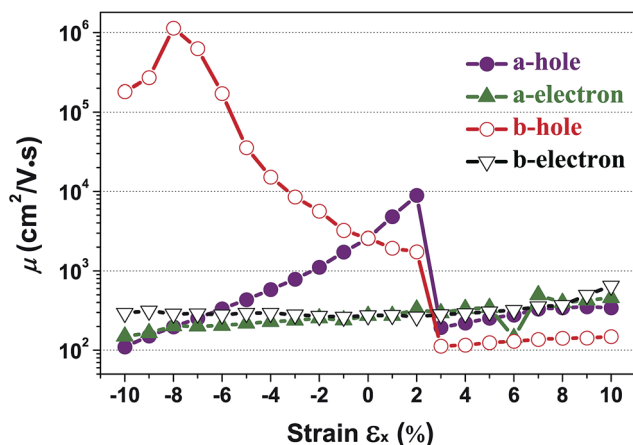

Fig. 6 The calculated charge carrier (hole and electron) mobility (μ) along the a- and b-directions as a function of the applied uniaxial strain, respectively.
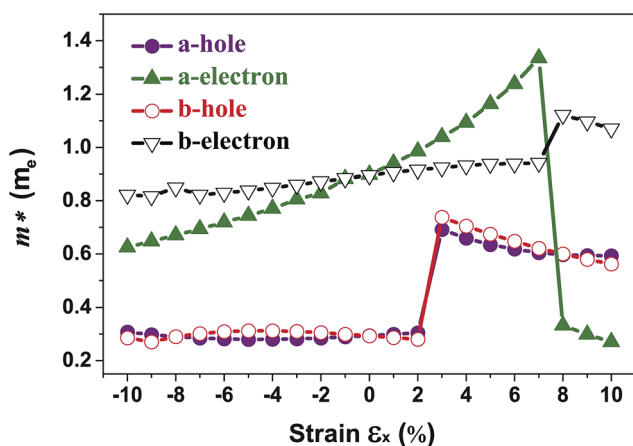

Fig. 7 The respective dependence of the calculated carrier (hole m_h^* and electron m_e^*) effective masses along the a- and b-directions on the applied uniaxial strains.
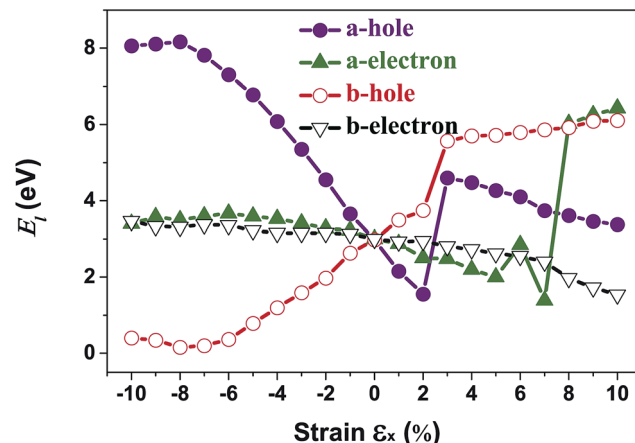

Fig. 8 The calculated carrier (hole and electron) deformation potential constant (E_l) along the a- and b-directions as a function of the applied uniaxial strain.

gap reaches a maximum value of 1.483 eV at the tensile strain of 1%.

Furthermore, to show the contribution of the different orbitals from the different atoms to the electronic states, we have calculated the total (DOS) and partial (PDOS) density of states for penta-SiC$_2$ with tensile and compressive strains: $\pm 10\%$ strains along the a-direction and the bi-direction, respectively, as shown in Fig. 4. By comparison, it's obvious that the contribution from the different orbitals of the Si and C atoms to the valence band does not change too much when uniaxial or biaxial strain is applied. However, when uniaxial or biaxial compressive strain around $\varepsilon_x = -10\%$ is applied, the contribution from the C-2p states becomes dominant in the energy range of 0 to 2 eV for the conduction band. Therefore, when monolayer penta-SiC$_2$ is free of strain or under tensile strain, the conduction band is mainly constructed of the low hybridization states of the Si-3p and C-2p orbitals, and when a large compressive strain is applied, the contribution from the C-2p states overwhelms that from the Si-3p states.

3.2 Strain-engineering mechanical properties of penta-SiC$_2$

Since monolayer penta-SiC$_2$ has nearly isotropic physical properties along the a- and b-directions, only the dependence on the strains of ε_x is considered in the following. Here, ε_x, ε_y and ε_{xy} refer to the components of the relative strain along the a-, b- and bi($a + b$)-directions, respectively. In addition, under the in-plane biaxial strain, the physical properties are nearly the same along the a- and b-directions, so only the physical properties along the b-direction are presented here. Due to three-dimensional (3D) periodic boundary conditions, the 2D elastic constant C_{ij}^{2D} should be rescaled by multiplying the c lattice parameter corresponding to the vacuum space between the 2D layers,[36] i.e., $C_{ij}^{2D} = c \times C_{ij}^{3D}$. The calculated in-plane elastic constant $C_{11}^{2D} = C_{22}^{2D} = 140$ N m^{-1} for penta-SiC$_2$ indicates that penta-SiC$_2$ nearly has isotropic mechanical properties. The positive values of C_{11}^{2D} and C_{22}^{2D} mean that penta-SiC$_2$ is mechanically stable, according to the mechanical stability

Table 2 The calculated carrier mobility of strained penta-SiC$_2$ in comparison to those of monolayer graphene, silicene, black phosphorene (BP) and MoS$_2$ (units of carrier mobility, cm^2 V^{-1} s^{-1})

Carrier mobility	Penta-SiC$_2$	Graphene[49]	Silicene[49]	BP[27,50]	MoS$_2$ (ref. 26 and 51)
Hole	1.14×10^6	3.51×10^5	2.23×10^5	286	200
Electron	649	3.39×10^5	2.58×10^5	2.2×10^3	72, ~200

criteria.[37] The 3D Young's modulus Y can be expressed as $Y = C_{ij}^{2D}/t$, where t is the effective thickness of the penta structure (4.8 Å for penta-SiC$_2$), and the calculated value of Y is 292 GPa for SiC$_2$, similar to that of MoS$_2$ (270 ± 100 GPa (ref. 19)), while it is larger than that of black phosphorene (179 GPa and 55 GPa along the a- and b-directions, respectively[38]), TiS$_3$ (96 GPa and 153 GPa along the a- and b-directions, respectively[24]) and HfS$_2$ (137 GPa (ref. 24)). The differences can be attributed to the bond length and the bond density of the different 2D materials.

Furthermore, we have calculated the elastic modulus along the a- and b-directions under various mechanical strains, as shown in Fig. 5. By stretching (compressing) the atom–atom bond length, the bond strength decreases (increases) in general due to less (more) overlap of the electron orbitals of the neighboring atoms, partly shown as the isosurface plots of the MLWFs in Fig. 2, which subsequently results in reducing (enlarging) the value of the elastic constants of the strained penta-SiC$_2$. Fig. 5(a) shows the dependence of the elastic constant along the a- and b-directions under uniaxial (ε_x) strain. Under uniaxial strain, the elastic constant decreases monotonously in the range of $-10\% \leq \varepsilon_x \leq 10\%$ along the b-direction, while along the a-direction, it has a maximum value at a tensile strain of $\varepsilon_x = 1\%$ and decreases linearly from $\varepsilon_x = 1\%$ to 10%, and under compressive strain, the elastic constant decreases linearly. While for biaxial strain as shown in Fig. 5(b), the value of the elastic modulus of the two directions decreases with a similar tendency to the b-direction under uniaxial strain for penta-SiC$_2$.

3.3 Strain-engineering transport properties of penta-SiC$_2$

The electron-phonon scatterings play a key role in determining the intrinsic electron transport properties of 2D materials. The deformation potential theory, proposed by Bardeen and Shockley,[39] sometimes overestimates the intrinsic mobility at room temperature since it only considers the coupling between electrons and longitudinal acoustic phonons in the long-wavelength limit.[40,41] However, it has been reported that the coupling intensity between electrons and acoustic phonons is about 3 times as large as that for the coupling between electrons and optic phonons,[42] therefore the carrier mobilities calculated by the deformation potential theory have been reported to be in good consistency with experiments for a series of two-dimensional materials.[26,43–45] In the long-wavelength limit, the carrier mobility of a two-dimensional material can be written as[26,41,46,47]

$$\mu = \frac{2e\hbar^3 C}{3k_B T |m^*|^2 E_l^2},\tag{1}$$

where e is the electron charge, T is the temperature (equal to 300 K throughout the paper), C is the elastic modulus of a uniformly deformed crystal by strain, and m^* is the effective mass given by $m^* = \hbar^2(\partial^2 E(k)/\partial k^2)^{-1}$ ($\hbar$ is the reduced Planck's constant, k is the wave-vector, and $E(k)$ denotes the energy). Also, E_l is the deformation potential (DP) constant defined by $E_l^{e(h)} = \Delta E_{CBM(VBM)}/(\delta l/l)$, where $\Delta E_{CBM(VBM)}$ is the energy shift of the band edge with respect to the vacuum level under a small dilation δl of the lattice constant l.

According to eqn (1), the carrier mobility of electrons and holes along certain directions for penta-SiC$_2$ is obtained, as shown in Fig. 6 and Table 3. Although the PBE calculations always underestimate the band gap, the calculated carrier mobilities are in good agreement with the experimental results for many 2D materials.[26,41,44,46,48] Firstly, we compared the a-

Table 3 The calculated effective mass m_b^* (with m_0^* being the static electron mass), the deformation potential constant E_{l-b}, the 2D elastic modulus C_b along the $\Gamma-Y$ direction and the electron/hole carrier mobility μ_b. The electron and hole carrier mobilities are calculated by using eqn (1) at $T = 300$ K

Carrier type	ε_{xy} [%]	m_b^* [m_0]	E_{l-b} [eV]	C_b [N m^{-1}]	μ_b [$\times 10^2$ cm^2 V^{-1} s^{-1}]	Carrier type	ε_{xy} [%]	m_b^* [m_0]	E_{l-b} [eV]	C_b [N m^{-1}]	μ_b [$\times 10^2$ cm^2 V^{-1} s^{-1}]
Hole	−10	0	0	0	0	Electron	−10	0	0	0	0
	−8	0.29	5.45	100.37	5.78		−8	0.67	3.66	100.37	2.24
	−6	0.30	4.78	118.29	8.43		−6	0.71	3.55	118.29	2.60
	−4	0.30	4.12	130.41	12.31		−4	0.75	3.47	130.41	2.72
	−2	0.30	4.03	137.66	13.68		−2	0.80	3.31	137.66	2.76
	0	0.29	2.99	139.89	25.88		0	0.90	3.0	139.89	2.74
	2	0.66	5.29	137.31	1.58		2	1.05	2.61	137.31	2.60
	4	0.55	4.80	130.34	2.65		4	1.30	1.81	130.34	3.30
	6	0.48	4.34	119.47	3.91		6	0.52	4.13	119.47	3.62
	8	0.43	4.00	106.01	4.99		8	0.46	3.96	106.01	4.44
	10	0.40	3.62	90.39	6.03		10	0.43	3.68	90.39	5.14

direction uniaxial strain modulated charge carrier mobility of penta-SiC$_2$ along the a- and b-directions, as shown in Fig. 6. Three different physical parameters, namely the carrier effective mass (m^*), the DP constant (E_l) and the elastic modulus (C), are subjected to change at a particular temperature under strain.

The band structures of strained penta-SiC$_2$ change when the structure changes, which subsequently alters the effective mass of the carriers determined by the curvatures of the band edges near the Fermi level. Fig. 7 demonstrates the evolution of the calculated effective masses of the electrons (m_e^*) and holes (m_h^*) along the a- and b-directions under uniaxial strains along the a-direction. The m_h^* at the S point is $0.29m_0$ and the m_e^* at the S–Γ point is $0.90m_0$ without strain (m_0 is the static electron mass).

As shown in Fig. 3(a), the applied strains along the a-direction ε_x may lead to large shifts of the positions of the VBMs and CBMs in the band structures. The VBM of penta-SiC$_2$ shifts from V_S to V_Γ with a strain of $\varepsilon_x = 3\%$, which results in a dramatic increase of the m_h^* ($0.30m_0 \rightarrow 0.69m_0$ along the a-direction and $0.28m_0 \rightarrow 0.74m_0$ along the b-direction) when ε_x increases from 2% to 3%. Meanwhile, the CBM of penta-SiC$_2$ shifts from $C_{S-\Gamma}$ to C_S with an applied strain of $\varepsilon_x = 8\%$. Therefore, a dramatic change of the electron effective mass occurs as well when the uniaxial strain changes from $\varepsilon_x = 7\%$ to $\varepsilon_x = 8\%$. The subsequent m_e^* reduces significantly from $1.33m_0$ to $0.33m_0$, and the b-direction m_e^* increases from $0.94m_0$ to $1.12m_0$, as shown in Fig. 7. Additionally, the anisotropic effective mass under strain will lead to anisotropic carrier mobilities, which finally lead to a direction-dependent electron conductivity.

In order to calculate the DP constant, a small dilation along a special direction needs to be applied. The calculated electron/hole DP constants for unstrained penta-SiC$_2$ are 3.00 eV and 2.98 eV, respectively, which are in good agreement with previous theoretical results.[33] Fig. 8 demonstrates the evolution of the electron (E_{l-e}) and hole (E_{l-h}) DP constants along the a- and b-directions under uniaxial strains along the a-direction. Similar to the case of the effective masses, the shifts of the VBMs with a uniaxial strain of $\varepsilon_x = 3\%$ and the CBMs with a strain of $\varepsilon_x = 8\%$ cause dramatic changes of the DP constants of the holes and electrons, respectively, as shown in Fig. 8. The nearly flat lines of E_{l-e} along the a-direction for ε_x ranging from -10% to -2%, and E_{l-h} along the a-direction for ε_x ranging from -10% to -8%, as shown in Fig. 8, can be understood by the nearly linear change of the CBM/VBM with ε_x changing in the corresponding ranges, as shown in Fig. 3(c). The reason is due to the fact that the electron/hole deformation potential constant along the a-direction is approximately the derivative of the CBM/VBM to the strain ε_x, i.e. $E_{l-e/h} \approx (E_{CBM/VBM}^{l+\delta l} - E_{CBM/VBM}^{l})/(\delta l/l)$.

Interestingly, the obtained b-direction E_{l-h} of the holes is low (0.15 eV → 0.40 eV) in the strain range of $-10\% \leq \varepsilon_x \leq 6\%$, which subsequently results in high hole-carrier mobilities larger than 10^5 cm^2 V^{-1} s^{-1} along a particular direction, as shown in Fig. 6.

The dependence of the calculated carrier mobilities on the uniaxial strain is shown in Fig. 6. The obtained hole and electron mobilities without strain are 2.59×10^3 cm^2 V^{-1} s^{-1} and 2.74×10^2 cm^2 V^{-1} s^{-1}, respectively. For uniaxial strain along

the a-direction, a dramatic enhancement of the hole mobility along the b-direction under compressive strains is observed, increasing from 2.59×10^3 cm^2 V^{-1} s^{-1} to 1.14×10^6 cm^2 V^{-1} s^{-1} at $\varepsilon_x = -8\%$. In Table 2, the calculated carrier mobilities of strained penta-SiC$_2$ and some widely-investigated two-dimensional semiconductors are listed. By comparison, it is found that the hole carrier mobility of penta-SiC$_2$ strained by $\varepsilon_x = -8\%$ is ultrahigh, being an order of magnitude higher than those of graphene (2.58×10^5 cm^2 V^{-1} s^{-1})[49] and silicene (3.39×10^5 cm^2 V^{-1} s^{-1}),[49] and three or four orders of magnitude higher than those of monolayer black phosphorene (2.2×10^3 cm^2 V^{-1} s^{-1})[27] and MoS$_2$ (~200 cm^2 V^{-1} s^{-1}),[26,51] which indicates that strain-engineering monolayer penta-SiC$_2$ is quite promising for the application of microelectronic devices. It should be noted that the available range of the compressive or tensile strain is determined by both the method to generate strains and the condition of the mechanical failure of strained materials.[52] Common strain-generating methods include lattice mismatch on the substrate, and thermal expansion or mechanical loading, which generally generate strains ranging from -12% to 25%.[53] Further stretching or compression should involve an investigation on the stability of strained materials.

It should be noted that strain-engineering has little influence on the electron mobility along both the a- and b-directions, as shown in Fig. 6. The hole mobility along the a-direction increases nearly linearly from 2.59×10^3 cm^2 V^{-1} s^{-1} to 1.0×10^4 cm^2 V^{-1} s^{-1} in the strain range of $\varepsilon_x = -10\%$ to 2%, which can be attributed to the monotonic decrease of the effective masses of the holes along the a-direction, according to eqn (1).

Table 3 shows the evolution of the effective mass (m_b^*), the DP constant (E_{l-b}), the elastic modulus (C_b) and the calculated results of the hole and electron mobilities along the b-direction under biaxial strains. For the hole mobility, as listed in Table 3, since all of the three decisive parameters (m_b^*, E_{l-b} and C_b) increase by applying tensile and compressive strain, the hole mobilities for the strained structures are thus smaller than that without strain according to eqn (1). The obtained electron mobility increases monotonically from $\varepsilon_{xy} = -10\%$ to $\varepsilon_{xy} = 10\%$, mainly caused by the decrease of the effective mass m_e^*.

4 Conclusion

In this paper, we have shown the evolution of the structure, electronic and charge carrier transport properties of penta-SiC$_2$ under uniaxial or biaxial strain, based on first-principles calculations. By calculation, it was found that monolayer penta-SiC$_2$ is a semiconductor with an indirect band gap of 2.85 eV (PBE: 1.39 eV). The transition from semiconductor to metal can take place when applying uniaxial or biaxial strains. The hole mobility along the b-direction can be greatly improved by applying a compressive strain along the a-direction. Meanwhile, strain-engineering has relatively little effect on the electron mobility. The novel and strain-modulated physical properties of monolayer penta-SiC$_2$ may lead to many potential applications in the fields of microelectronic and optoelectronic devices.

Conflicts of interest

There are no conflicts to declare.

Acknowledgements

References

1 K. S. Novoselov, A. K. Geim, S. V. Morozov, D. Jiang, Y. Zhang, S. V. Dubonos, I. V. Grigorieva and A. A. Firsov, *Science*, 2004, **306**, 666–669.

2 K. S. Novoselov, A. K. Geim, S. V. Morozov, D. Jiang, M. I. Katsnelson, I. V. Grigorieva, S. V. Dubonos and A. A. Firsov, *Nature*, 2005, **438**, 197–200.

3 Y. Zhang, Y.-W. Tan, H. L. Stormer and P. Kim, *Nature*, 2005, **438**, 201–204.

4 X. Zhang, H. Zhang, C. Li, K. Wang, X. Sun and Y. Ma, *RSC Adv.*, 2014, **4**, 45862–45884.

5 A. A. Alandin, *Nat. Mater.*, 2011, **10**, 569–581.

6 A. A. Balandin, S. Ghosh, W. Bao, I. Calizo, D. Teweldebrhan, F. Miao and C. N. Lau, *Nano Lett.*, 2008, **8**, 902–907.

7 F. Schedin, A. K. Geim, S. V. Morozov, E. W. Hill, P. Blake, M. I. Katsnelson and K. S. Novoselov, *Nat. Mater.*, 2007, **6**, 652–655.

8 S. Balendhran, S. Walia, H. Nili, S. Sriram and M. Bhaskaran, *Small*, 2015, **11**, 640–652.

9 K. Zhou, S. Jiang, C. Bao, L. Song, B. Wang, G. Tang, Y. Hu and Z. Gui, *RSC Adv.*, 2012, **2**, 11695–11703.

10 G. Wang, R. Pandey and S. P. Karna, *ACS Appl. Mater. Interfaces*, 2015, **7**, 11490–11496.

11 S. Zhang, J. Zhou, Q. Wang, X. Chen, Y. Kawazoe and P. Jena, *Proc. Natl. Acad. Sci. U. S. A.*, 2015, **112**, 2372–2377.

12 W. Xu, G. Zhang and B. Li, *J. Chem. Phys.*, 2015, **143**, 154703.

13 H. Liu, G. Qin, Y. Lin and M. Hu, *Nano Lett.*, 2016, **16**, 3831–3842.

14 G. R. Berdiyorov and M. E.-A. Madjet, *RSC Adv.*, 2016, **6**, 50867–50873.

15 Y. Aierken, O. Leenaerts and F. M. Peeters, *Phys. Chem. Chem. Phys.*, 2016, **18**, 18486–18492.

16 A. Lopez-Bezanilla and P. B. Littlewood, *J. Phys. Chem. C*, 2015, **119**, 19469–19474.

17 K. Novoselov and A. C. Neto, *Phys. Scr.*, 2012, **2012**, 014006.

18 M. Ghorbani-Asl, S. Borini, A. Kuc and T. Heine, *Phys. Rev. B: Condens. Matter Mater. Phys.*, 2013, **87**, 235434.

19 S. Bertolazzi, J. Brivio and A. Kis, *ACS Nano*, 2011, **5**, 9703–9709.

20 A. Castellanos-Gomez, M. Poot, G. A. Steele, H. S. van der Zant, N. Agraït and G. Rubio-Bollinger, *Adv. Mater.*, 2012, **24**, 772–775.

21 J. Feng, X. Qian, C. W. Huang and J. Li, *Nat. Photonics*, 2012, **6**, 866–872.

22 H. J. Conley, B. Wang, J. I. Ziegler, J. Richard, F. Haglund, S. T. Pantelides and K. I. Bolotin, *Nano Lett.*, 2013, **13**, 3626–3630.

23 S. Yu, H. Zhu, K. Eshun, C. Shi, M. Zeng and Q. Li, *Appl. Phys. Lett.*, 2016, **108**, 191901.

24 J. Kang, H. Sahin and F. M. Peeters, *Phys. Chem. Chem. Phys.*, 2015, **17**, 27742–27749.

25 G. Phan, K. Nakayama, K. Sugawara, T. Sato, T. Urata, Y. Tanabe, K. Tanigaki, F. Nabeshima, Y. Imai, A. Maeda, et al., *Phys. Rev. B: Condens. Matter Mater. Phys.*, 2017, **95**, 224507.

26 Y. Cai, G. Zhang and Y. Zhang, *J. Am. Chem. Soc.*, 2014, **136**, 6269–6275.

27 R. Fei and L. Yang, *Nano Lett.*, 2014, **14**, 2884–2889.

28 D. Ã. Yierpan Aierken and F. M. Peeters, *Phys. Chem. Chem. Phys.*, 2016, **18**, 14434–14441.

29 G. Kresse and J. Furthmüller, *Phys. Rev. B: Condens. Matter Mater. Phys.*, 1996, **54**, 11169–11186.

30 J. Heyd, G. E. Scuseria and M. Ernzerhof, *J. Chem. Phys.*, 2003, **118**, 8207–8215.

31 A. A. Mostofi, J. R. Yates, Y.-S. Lee, I. Souza, D. Vanderbilt and N. Marzari, *Comput. Phys. Commun.*, 2008, **178**, 685–699.

32 N. Marzari, A. A. Mostofi, J. R. Yates, I. Souza and D. Vanderbilt, *Rev. Mod. Phys.*, 2012, **84**, 1419–1475.

33 X. Li, Y. Dai, M. Li, W. Wei and B. Huang, *J. Mater. Chem. A*, 2015, **3**, 24055–24063.

34 W. Zhou, M. D. Kapetanakis, M. P. Prange, S. T. Pantelides, S. J. Pennycook and J.-C. Idrobo, *Phys. Rev. Lett.*, 2012, **109**, 206803.

35 V. O. Özçelik, O. U. Aktürk, E. Durgun and S. Ciraci, *Phys. Rev. B: Condens. Matter Mater. Phys.*, 2015, **92**, 125420.

36 M. N. Blonsky, H. L. Zhuang, A. K. Singh and R. G. Hennig, *ACS Nano*, 2015, **9**, 9885–9891.

37 B. Peng, H. Zhang, H. Shao, Z. Ning, Y. Xu, G. Ni, H. Lu, D. W. Zhang and H. Zhu, *Mater. Res. Lett.*, 2017, **5**, 399–407.

38 Q. Wei and X. Peng, *Appl. Phys. Lett.*, 2014, **104**, 251915.

39 J. Bardeen and W. Shockley, *Phys. Rev.*, 1950, **80**, 72–80.

40 Y. Nakamura, T. Zhao, J. Xi, W. Shi, D. Wang and Z. Shuai, arXiv preprint arXiv:1705.01816, 2017.

41 J. Chen, J. Xi, D. Wang and Z. Shuai, *J. Phys. Chem. Lett.*, 2013, **4**, 1443–1448.

42 L. Tang, M. Long, D. Wang and Z. Shuai, *Sci. China, Ser. B: Chem.*, 2009, **52**, 1646–1652.

43 R. Wang, B. A. Ruzicka, N. Kumar, M. Z. Bellus, H.-Y. Chiu and H. Zhao, *Phys. Rev. B: Condens. Matter Mater. Phys. B*, 2012, **86**, 045406.

44 J. Xi, M. Long, L. Tang, D. Wang and Z. Shuai, *Nanoscale*, 2012, **4**, 4348–4369.

45 S. V. Morozov, K. S. Novoselov, M. I. Katsnelson, F. Schedin, D. C. Elias, J. A. Jaszczak and A. K. Geim, *Phys. Rev. Lett.*, 2008, **100**, 16602.

46 M. Long, L. Tang, D. Wang, Y. Li and Z. Shuai, *ACS Nano*, 2011, **5**, 2593–2600.

47 Y. Wang and Y. Ding, *Nanoscale Res. Lett.*, 2015, **10**, 254.

48 J. Dai and X. C. Zeng, *Angew. Chem.*, 2015, **127**, 7682–7686.

49 Z.-G. Shao, X.-S. Ye, L. Yang and C.-L. Wang, *J. Appl. Phys.*, 2013, **114**, 093712.

50 J. Liu, G.-M. Choi and D. G. Cahill, *J. Appl. Phys.*, 2014, **116**, 233107.

51 S. Kim, A. Konar, W.-S. Hwang, J. H. Lee, J. Lee, J. Yang, C. Jung, H. Kim, J.-B. Yoo, J.-Y. Choi, *et al.*, *Nat. Commun.*, 2012, **3**, 1011.

52 S. Liu, B. Liu, X. Shi, J. Lv, S. Niu, M. Yao, Q. Li, R. Liu, T. Cui and B. Liu, *Sci. Rep.*, 2017, **7**, 2404.

53 K. S. Kim, Y. Zhao, H. Jang, S. Y. Lee, J. M. Kim, K. S. Kim, J.-H. Ahn, P. Kim, J.-Y. Choi and B. H. Hong, *Nature*, 2009, **457**, 706.